

## Test particle analysis in L- and H-mode simulations

G. Sánchez Burillo,<sup>1</sup> B. Ph. van Milligen,<sup>1</sup> and A. Thyagaraja<sup>2</sup>

<sup>1</sup>Asociación EURATOM-CIEMAT para Fusión, Laboratorio Nacional de Fusión, Avda. Complutense 22, 28040 Madrid, Spain

<sup>2</sup>EURATOM-CCFE Fusion Association, Culham Science Centre, Abingdon OX14 3DB, United Kingdom

(Received 14 January 2010; accepted 23 March 2010; published online 7 May 2010)

In this work, the radial transport of tracers in an H-mode run in the CUTIE code [A. Thyagaraja *et al.*, Phys. Plasmas **12**, 090907 (2005)] is analyzed globally. Several techniques are applied to the study of the trajectories performed by the tracers, measuring the degree of self-similarity in the motion and searching for long range spatial and temporal correlations. The results are compared to those of an L-mode run [G. Sánchez Burillo *et al.*, Phys. Plasmas **16**, 042319 (2009)] in order to highlight the changes between L and H. The analysis of self-similarity parameters of the motion reveals that changes, if any, are slight, although the reliability of the results is limited. Nevertheless, the study of the mean step size indicates that transport is more local (or rather less global) and the anomalous diffusion contribution is less dominant. Namely, the variance of the radial distribution of tracers is smaller in H-mode and the strong asymmetry in the positive/negative steps performed by the tracers vanishes. © 2010 American Institute of Physics. [doi:10.1063/1.3392290]

### I. INTRODUCTION

The analysis of the trajectories of test particles (tracers) is a powerful tool for characterizing transport in complex systems, including anomalous transport in tokamaks. In Ref. 1, this technique was used to study radial transport in the turbulence code CUTIE (Ref. 2) in an L-mode simulation. In the present work, this study is expanded to an H-mode simulation, and a comparison is made between transport parameters in the two plasma states.

The analysis performed here applies the same basic approach as other works.<sup>3-9</sup> The novelty here is that CUTIE provides a full-tokamak simulation of turbulent transport. In Sec. II, we briefly describe the methods used, in Sec. III we present the results, and in Sec. IV we provide a discussion and some conclusions.

### II. METHODS

#### A. The continuous time random walk

Anomalous transport in magnetic confinement devices is only partly understood. It has been suggested that the anomalous component of radial transport (i.e., the part not predicted by neoclassical estimates, which is often a significant, if not dominant, fraction of the total transport) can best be modeled in the framework of the probabilistic continuous time random walks<sup>10,11</sup> (CTRWs) since long range correlations in both space and time appear to play a significant part. In a CTRW model, particle motion is described by an alternating succession of (instantaneous) “steps” and “waiting times,” during which the particle does not move. While the formalism is quite general, it is common to assume that the probability distribution functions (pdfs) of steps,  $p(\Delta x)$ , and waiting times,  $\psi(\Delta t)$ , are independent.<sup>12</sup> A generalized master equation (GME) can then be derived for the time evolution of the particle density.<sup>13,14</sup> It is also common to assume that the mentioned steps and waiting times refer to mesos-

copic processes, which are the result of the sum of independent and random microscopic processes. In this case, the generalized central limit theorem<sup>15</sup> applies so that  $p(\Delta x)$  and  $\psi(\Delta t)$  must be stable Lévy distributions. Typically,  $p(\Delta x)$  will be a symmetric (not necessarily Gaussian) Lévy pdf and  $\psi(\Delta t)$  a fully asymmetric (not necessarily exponential) one. These distributions have a large-scale behavior given by  $p(\Delta x) \propto \Delta x^{-1-\alpha}$  and  $\psi(\Delta t) \propto \Delta t^{-1-\beta}$ , where  $0 < \alpha < 2$  and  $0 < \beta < 1$ , while the cases  $\alpha=2$  and  $\beta=1$  are special and correspond to the Gaussian and exponential distributions, respectively. Subject to the cited assumptions, the GME tends to a so-called fractional differential equation in the fluid limit,<sup>16,17</sup> and can be identified with the standard diffusion equation when  $\alpha=2$  and  $\beta=1$ .

Several techniques are available to determine  $\alpha, \beta$  and  $H=\beta/\alpha$  from particle distributions and trajectories<sup>3-6</sup> The determination of these parameters then allows classifying the transport and deciding whether the *effective* transport is standard (diffusive), subdiffusive, or superdiffusive, or some combination.

#### B. Simulations using CUTIE

CUTIE is a full-tokamak, quasineutral, two-fluid code incorporating electromagnetic turbulence.<sup>2,18,19</sup> Here, the parameters are chosen to match the COMPASS-D tokamak (now operating at Prague<sup>20</sup>). The geometry of the system is a periodic cylinder (here  $r$  is the radial,  $\theta$  is the “poloidal,” and  $\phi=z/R$  is the “toroidal” coordinates), although toroidicity effects are included.

The code computes the following fields: electron and ion temperatures ( $T_e$  and  $T_i$ , different in general), density (using quasineutrality, we take the number density  $n=n_e \approx Z_{\text{eff}} n_i$ ), ion velocity ( $\mathbf{v}_i$ ), electrostatic potential ( $\Phi$ ), and vector potential ( $\Psi$ ).<sup>21-23</sup> Consequently, the dynamics in CUTIE includes several unstable (ideal and viscoresistive) modes. Mesoscale physics are modeled, and profiles and turbulence

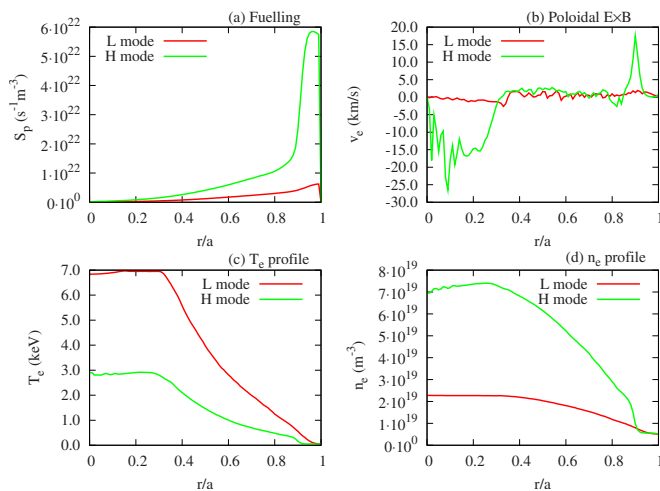


FIG. 1. (Color online) L-H-mode transition.

coevolve self-consistently. Therefore, the code seems suited for the mesoscale analysis offered by the method described above, while the coevolution of turbulence and profiles leads one to expect nontrivial results associated with self-organization.

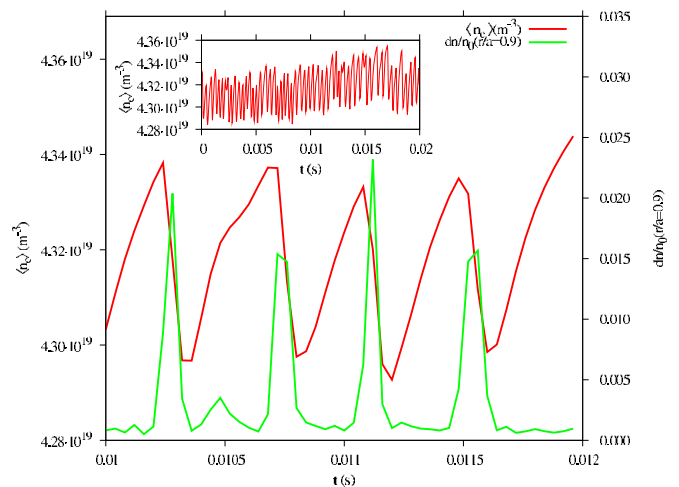
### C. The CUTIE H-mode

In CUTIE, the mean density is controlled by a straightforward feedback mechanism and an externally imposed target density  $\bar{n}_{\text{target}}$ . Whenever the calculated line-average density is such that  $\bar{n} < \bar{n}_{\text{target}}$  the source is activated with a general form  $S_p \propto S(r/a)(\bar{n}_{\text{target}} - \bar{n})$ , where  $S(r)$  is a fixed profile peaking at  $r/a = 0.95$ . For a low value of the feedback control density ( $\bar{n} = 1.8 \times 10^{19} \text{ m}^{-3}$ ), the code is in L-mode. When the feedback density is set to  $\bar{n} = 5.3 \times 10^{19} \text{ m}^{-3}$ , the fuelling rate increases by one order of magnitude. As the density is raised, the plasma makes a transition to a state that bears some similarity to an H-mode. For simplicity, we will refer to this state by this term in the remainder of the paper.

As important as the feedback mechanism is the particle sink in the region  $r/a > 0.95$ . This fact together with the particle source enhances the density gradient just inside the “separatrix,” which has been suggested to be the responsible for the transition.<sup>24</sup>

The radial profile of the poloidal velocity reflects the formation of a typical H-mode shear layer near  $\rho = 0.85$ , associated with an external transport barrier (ETB). Reynolds stress plays an important role in the formation of this barrier by driving the poloidal flow significantly above neoclassical levels. In addition, temperature and density profiles show the typical H-mode pedestal (Fig. 1). These changes occur within a few microseconds after increasing the feedback density  $\bar{n}$ . On the other hand, the safety factor profile does not change significantly. 10–15 ms later, quasiperiodic edge relaxations (pedestal) set in. At this time, we consider that the full L-mode to ELMy (i.e., with ELMs) H-mode transition has been completed, and this final state will be subjected to analysis in the following.

Note that the input electron cyclotron resonant heating power is kept constant. Thus, the strong increase in density

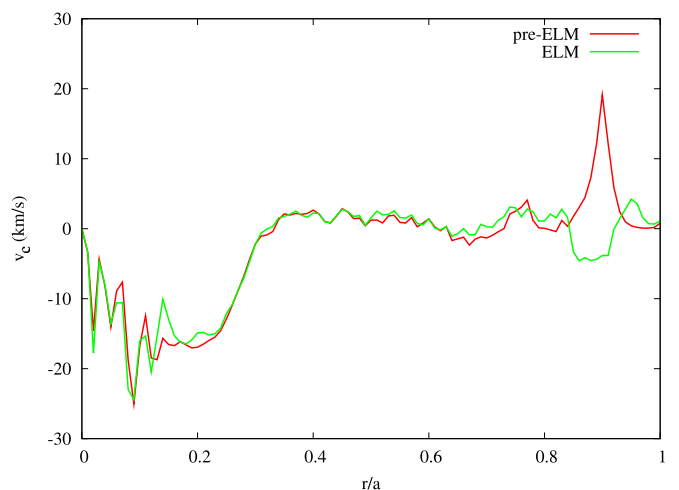
FIG. 2. (Color online) Quasiperiodic oscillations of  $\langle n_e \rangle$  and  $dn/n_0(r/a=0.9)$ , reflecting the ELM frequency and their wave form (plotted at 40  $\mu\text{s}$  intervals).

leads to a concomitant decrease in electron temperature. Inside the pedestal region ( $r/a < 0.8$ ), the profiles are not much affected by the edge localized modes (ELMs) but the line-averaged density fluctuates slightly as a consequence of these relaxations. See Fig. 2.

From Fig. 2 one may deduce that the ELM period is approximately  $\tau_{\text{ELM}} \sim 0.36$  ms. The radial profile of the poloidal  $E \times B$  velocity reflects the impact of the ELMs on the ETB. See Fig. 3.

The effect of the ELMs is clearly seen in the local density oscillations. Figure 4 shows that the H-mode oscillations are strongly enhanced in the edge region during the ELMs, as compared to the L-mode case, characterized by quasiperiodic oscillations of much smaller amplitude and without a clear shear layer.

In the midradius region ( $0.4 < r/a < 0.7$ , approximately) the radial propagation of the edge-induced oscillations is observed in both cases. However, in L-mode, these fluctuations propagate faster ( $v_H \approx 14.5$  m/s and  $v_L \approx 19.2$  m/s). An-

FIG. 3. (Color online) ETB relaxation during ELMs:  $E \times B$  poloidal velocity 40  $\mu\text{s}$  before the ELM and during the ELM.

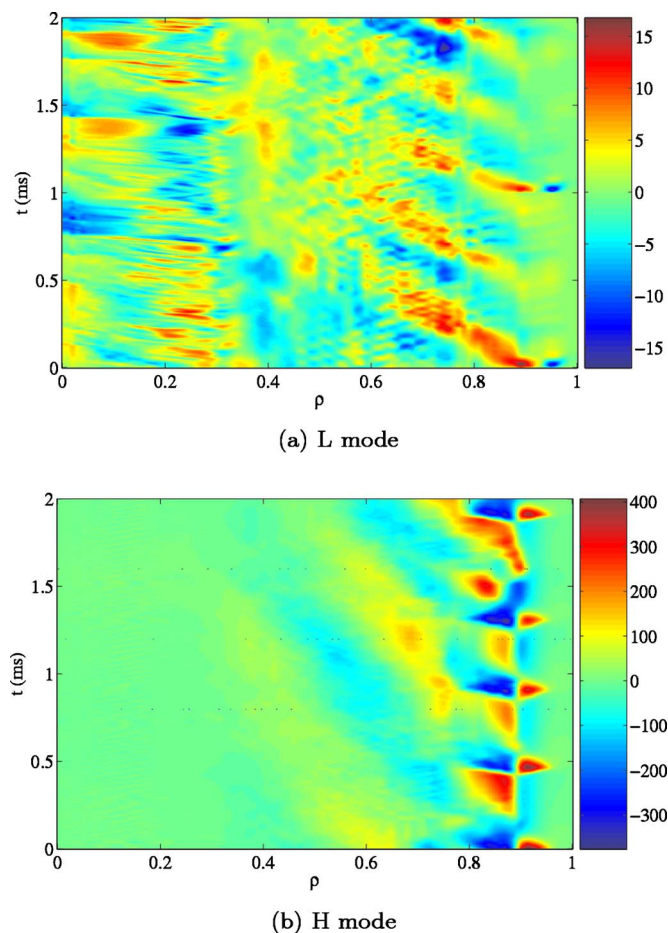


FIG. 4. (Color online) Electron density fluctuations in units of  $10^{10} \text{ cm}^{-3}$ .

other important difference is the deeper penetration of the H-mode oscillations that propagate down to  $r/a \approx 0.4$ , while in L-mode they only reach  $r/a \approx 0.6$ .

In view of Fig. 4, one may distinguish different radial regions in the simulation, indicating different local underlying physics. For instance, in the plasma edge there is a transport barrier at  $r/a \sim 0.9$ , and immediately inside there is a wide radial range where density perturbations appear to propagate ballistically. Intuitively, a transport barrier might be expected to cause subdiffusive transport,<sup>8</sup> while ballistic transport might be associated with superdiffusion. However, such intuition may be misleading, and the current work will attempt to shed some light on this issue. While the existence of radial regions with distinct transport characteristics might seem to be incompatible with a global description of transport in terms of a CTRW, the effective global transport might still be modeled in terms of Lévy distributions, depending on the distribution of such zones and the microscopic behavior of tracer motion. Indeed, in the L-mode reference case, this clearly seemed to be the case.<sup>1</sup> Further details on the L-H transition and the H-mode in CUTIE can be found in Ref. 24.

#### D. Tracers in CUTIE

In this study, the injected tracers move according to the local fluid velocity. The tracers are ideal, i.e., they have neither mass nor charge. Thus, the obtained results reflect the

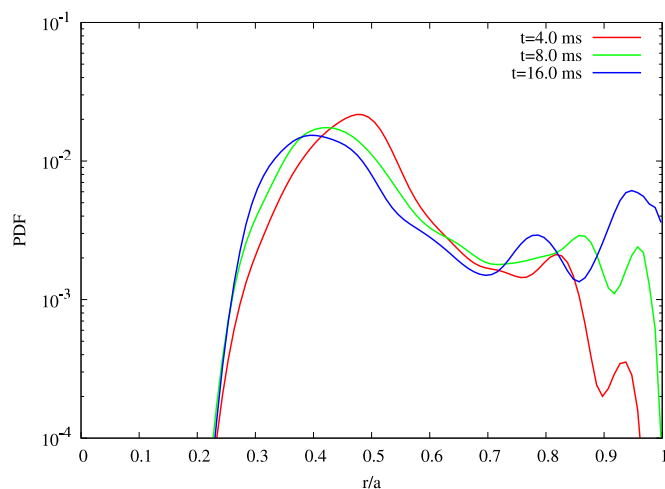


FIG. 5. (Color online) Propagator in the H-mode: 4, 8, and 16 ms after being launched at  $r/a=0.5$ .

flow lines of the fluid flow but do not reflect the motion of realistic particles. For accuracy, the Fourier oversampling of the three dimensional grid (3D) (in the  $z$  direction) and a 3D spline technique are used to interpolate the velocity field. The tracer trajectories are obtained by integrating the velocity, using an Eulerian scheme.

Once the ELMy H-mode is established, 10 000 tracer particles are injected into the system. Tracers are launched simultaneously at  $r/a=0.5$  and randomly distributed in  $\theta$  and  $z$ . The tracers are followed for  $\tau_{\text{sim}}=20$  ms, i.e., approximately five to seven times longer than the particle confinement time,  $\tau_p \approx 3-4$  ms.

### III. RESULTS

In this section, the tracer trajectories in the H-mode are analyzed and compared to the L-mode results.

#### A. The propagator

The definition of propagator  $P(r/a)$  we use here is simply the radial distribution (or histogram) of the tracers. This simple definition only corresponds to its mathematical counterpart in the limit of small times and many particles. In Fig. 5 we show the propagator at times  $t=4.0, 8.0,$  and  $16.0$  ms. In Fig. 6 we plot the H- and L-mode propagators.

Figure 6 again shows significantly different behaviors of tracers in the L- and H-mode runs (cf. also Ref. 1). (i) Drifts are opposite: inward and outward in the H- and L-modes, respectively. (ii) The distribution is narrower in the H-mode than in the L-mode. If  $\sigma$  is the variance (width) of the distribution at a given time, then  $\sigma_L^2 \sim 2\sigma_H^2$ . (iii) The ELM relaxation ejects the tracers to locations beyond the transport barrier at  $r/a \approx 0.81$ , which is a nearly insurmountable obstacle for the test particles in the L-mode run. Another transport barrier exists around  $r/a \approx 0.3$ , associated with the  $q=1$  rational surface.

Although the propagator is clearly asymmetric, part of this asymmetry is simply due to the drift in combination with the finite size of the system, leading to a deformation of  $P$ . Focusing on the longest tail of the propagator (in the

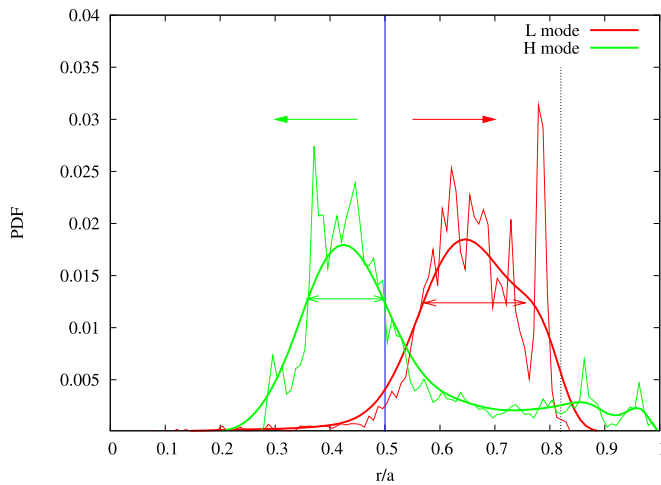


FIG. 6. (Color online) Propagator in L- and H-modes, 8 ms after being launched at  $r/a=0.5$ .

opposite direction of the drift), one can try to determine the decay index [assuming  $P(\Delta\rho) \propto (|\Delta\rho|^{-1-\alpha})$ , where  $\Delta\rho = (r-r_0)/a$ ]. In the L-mode, this method leads to a more or less reasonable estimate of  $\alpha$ . However, in the H-mode, the tail does not stand out clearly due to an apparent accumulation of particles for large values of  $|\Delta\rho|$  (Fig. 7), possibly due to a finite-size effect: Apparently, radial particle excursions are larger, on average, in H-mode, so that the finite-size effect (deformation of the distribution to boundary effects) is more prominent. This is consistent with the mean step size values shown in Fig. 20.

In order to quantify the decay index, the distribution should have an objective power-law decay range with sufficient length. Somewhat arbitrarily, but in accordance with custom, the power-law decay should at least be 1 decade long in order to be considered significant. For a fit to a power law  $f(x) = |x-x_0|^{-1-\alpha}$  valid in the range  $x_1 < x < x_2$ , the fit length is defined as

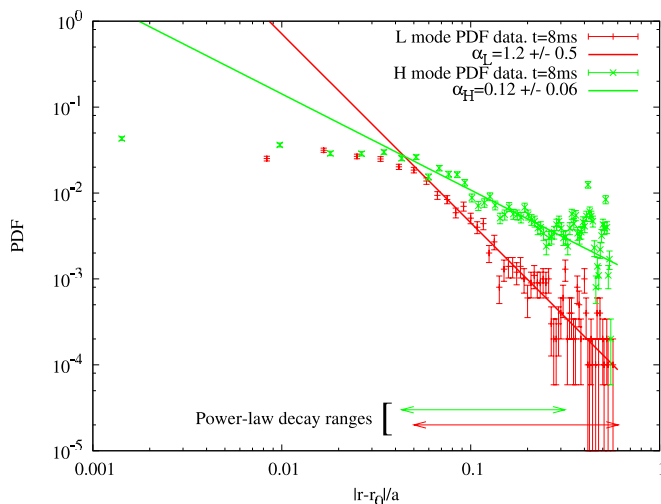


FIG. 7. (Color online) PDF fits to a power law in L- and H-modes.

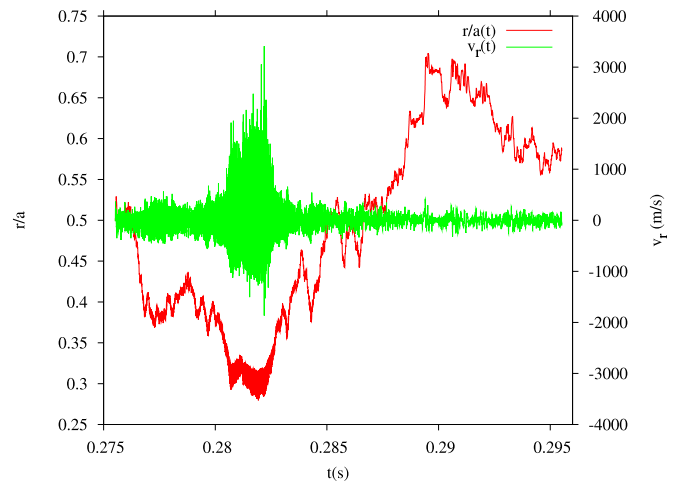


FIG. 8. (Color online) Radial position and velocity of a single tracer.

$$L_{\text{fit}} = \log_{10} \left( \frac{|x_2 - x_0|}{|x_1 - x_0|} \right). \quad (1)$$

In this case, the fit length in the L-mode is larger than a decade:  $L_{\text{fit,L}} = 1.1$ , while in H-mode, it is smaller:  $L_{\text{fit,H}} = 0.8$ . This is a further argument indicating that the L-mode value,  $\alpha_L = 1.2 \pm 0.5$ , although only marginally significant, is reliable, while the H-mode value is not.

## B. Step and waiting time distributions

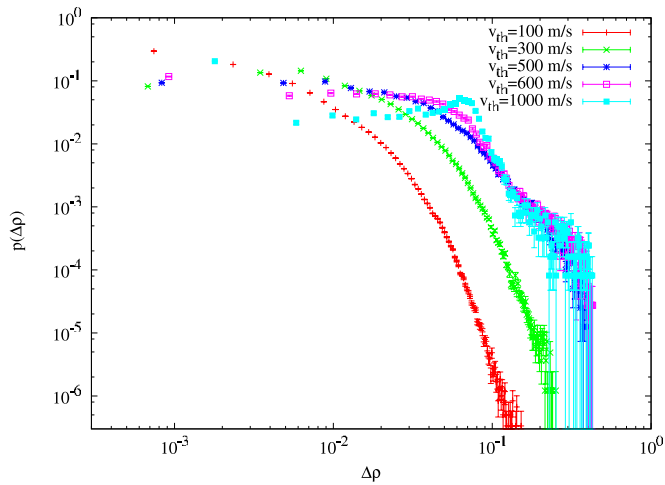
As described in Ref. 1, the continuous motion can be artificially decomposed into steps and waiting times, thus allowing the computation of radial step size and waiting time pdfs. These distributions contain all the information necessary to describe the motion from the CTRW point of view.

This decomposition is based on a velocity threshold  $v_{\text{th}}$ . The particle is assumed to perform a jump when its absolute radial velocity exceeds this threshold, and else it is considered to be “trapped” (waiting). The computation of the pdfs is straightforward but depends on the choice of the arbitrary threshold. Therefore, a range of thresholds should be explored, and the results, if significant, should be relatively insensitive to the precise choice of  $v_{\text{th}}$  in a subrange. The value of the parameters obtained in this subrange, if it exists, is considered to constitute a meaningful result.

In the core region,  $r/a \leq 0.35$ , the radial velocities far exceed those of the range  $0.35 < r/a < 1$  (by a factor of 10, cf. Fig. 8). It is therefore necessary to treat these ranges separately and we focus on the latter range since that is where the majority of particles are. This is also the range where the L-mode analysis was performed.

### 1. Step pdf

A sequence of step size distributions for different  $v_{\text{th}}$  is shown in Fig. 9. As the threshold is increased, the tail of the distribution rises, as expected (since large jumps become ever more important), but no clear power-law decay region is detected. Again, this is attributed to the fact that the mean value of the steps is larger in H-mode so that the finite-size effect deforming the pdf is more important.

FIG. 9. (Color online) H-mode step size pdfs for different  $v_{th}$ .

In our previous work, we found that one could fit the pdf to a power-law function in L-mode (despite the finite-size effect). Using an *ad hoc* fit function consisting of three connected intervals with exponential, power law, and exponential decay, and imposing continuity, the whole pdf could be fitted satisfactorily (Fig. 10). Using  $v_{th}=500$  m/s, the same fit was attempted in H-mode, yielding  $\alpha \approx 2.00 \pm 0.25$ .

Around  $v_{th}=300$  m/s, the L-mode fit result was least sensitive to  $v_{th}$  while simultaneously optimizing the value of  $\chi^2$  of the fit. The H-mode distribution, on the contrary, evolves continuously as a function of the threshold parameter (Figs. 9 and 11): It decays exponentially for low  $v_{th}$ , while an exponential-algebraic-exponential fit is reasonably successful for  $v_{th}=500$  m/s, but for higher thresholds the finite-size effect dominates, and in addition the pdf peaks at  $\Delta\rho \sim 0.06-0.07$ , and it is not possible to perform a fit using such simple functions.

In summary, there is no threshold range where the dependence of  $\alpha$  on  $v_{th}$  vanishes. Due to the cited evolution with  $\alpha$  and the onset of finite-size effects, we cannot determine a reliable value for  $\alpha$  using this method.

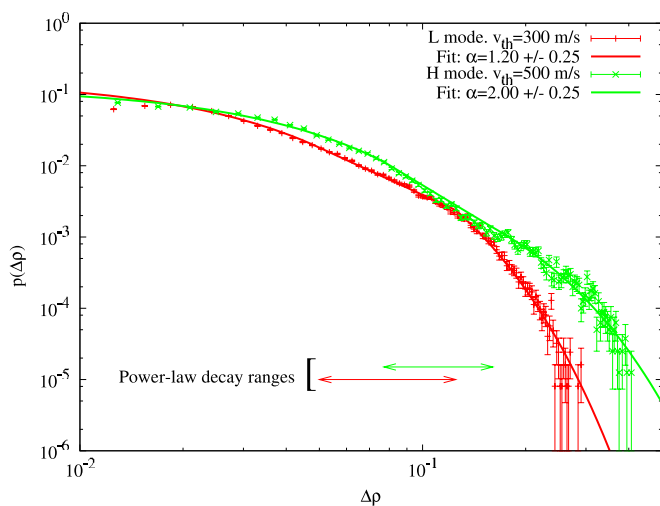


FIG. 10. (Color online) Best fits in L- and H-mode step size pdfs.

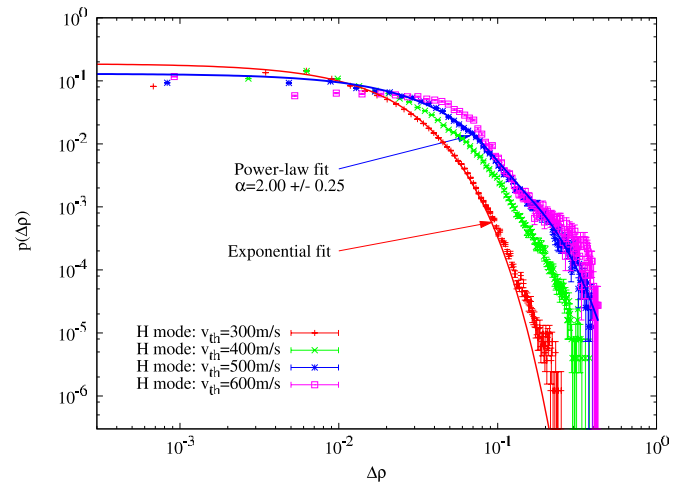


FIG. 11. (Color online) H-mode steps pdfs and fits: exponential and power law.

## 2. Waiting time pdf

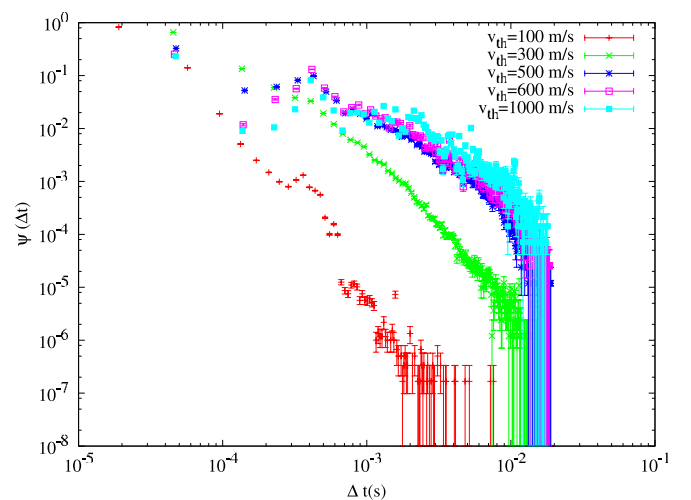
The waiting time distribution is shown in Fig. 12, also for different thresholds. Note the peak at  $\Delta t = 0.4$  ms, associated with the ELM period. Again, the tail rises as the threshold is increased.

The aim of this technique is to fit the distribution to a power-law function  $\psi(\Delta t) \propto \Delta t^{-1-\beta}$ , with  $0 < \beta < 1$ . In this case, there seems to exist a  $\Delta t$  range where, for large  $v_{th}$ , the fit is feasible, see Fig. 13.

The L- and H-mode results are quite similar:  $\beta_H \approx 0.59 \pm 0.03$ ,  $\beta_L \approx 0.51 \pm 0.04$ . However, the fit in the L-mode case is more robust, as is evident from simple inspection of the data. In order to quantify this, we note that the fit length [cf. Eq. (1)] is longer in L-mode ( $L_{fit,L} = 2.0$ ) than in H-mode ( $L_{fit,H} = 0.9$ ).

## C. Radial velocity correlations

The Lagrangian velocity of the tracer particles can be studied by means of the *rescaled range* (RS) and *structure function* (SF) diagnostics. These techniques measure the

FIG. 12. (Color online) H-mode waiting time pdfs for different  $v_{th}$ .

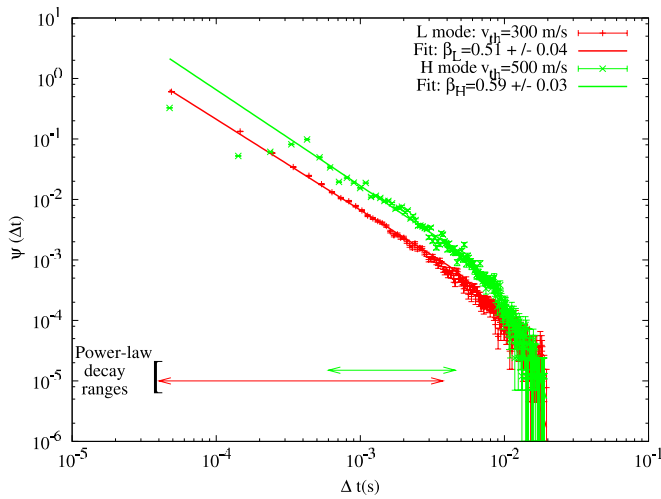


FIG. 13. (Color online) L- and H-mode waiting time pdfs and fits.

Lagrangian correlation and the so-called Hurst exponent  $H \equiv \beta/\alpha$ .

**1. RS**

The RS analysis<sup>25</sup> is applied to the radial velocity of the tracers. There is a “mesoscale” time range (longer than the decorrelation time of turbulence but shorter than the confinement time) where the RS function is expected to scale as  $RS(\tau) \propto \tau^H$ . This diagnostic can be used with every single particle, see Fig. 14.

The RS function is calculated for each of the 10 000 tracers. The dots are fitted to a curve consisting of two connected power laws. At large values of  $\tau$  the curve saturates, but these values are not taken into consideration since the statistics are very poor in that region. For low values of  $\tau$ ,  $H \approx 1$  (the “ballistic” region, associated with deterministic motion prior to the onset of randomization). The interesting part of the curve occurs for intermediate values of  $\tau$  (the “inertial” region), which is where we compute  $H$ . Averaging over the tracers we obtain  $\langle H \rangle = 0.55 \pm 0.06$ . This is, within the error, a diffusive result and quite similar to the L-mode result ( $\langle H \rangle = 0.54 \pm 0.05$ ).

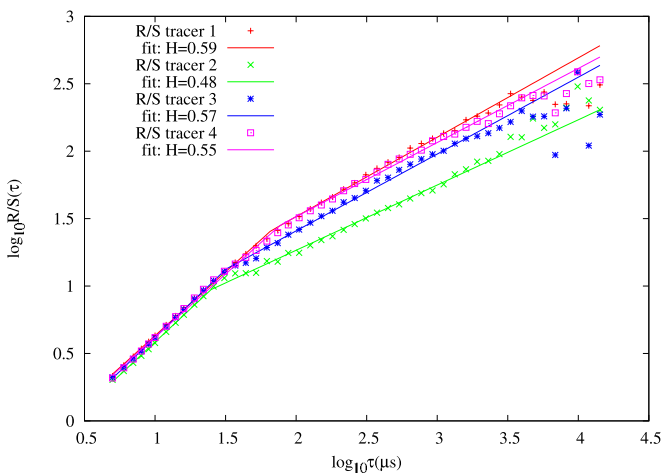


FIG. 14. (Color online) Examples of RS for single tracers and fits.

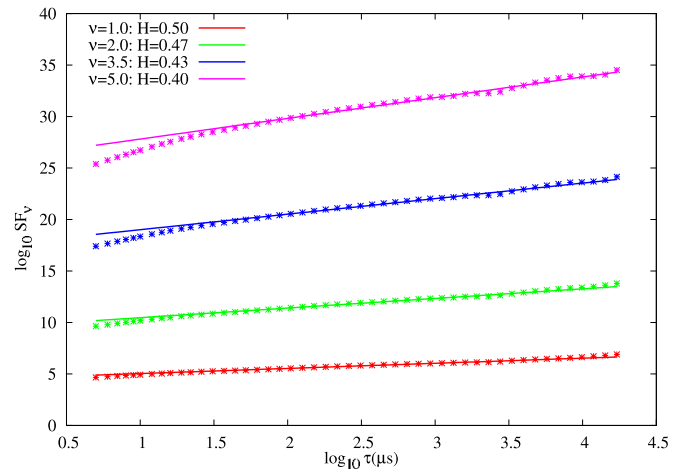


FIG. 15. (Color online) Type I SFs for a single tracer, with different  $\nu$ 's and fits.

The time  $\tau_H$ , being the time of the first slope change, is  $\tau_H \sim 30 \mu s$ , while in L-mode it is much higher,  $\tau_L \sim 100 \mu s$ . This is an indication that the turbulence decorrelation time is much shorter in H-mode.

**2. SF**

The SFs  $SF_\nu$  for different  $\nu$  orders were also computed. In a certain range of  $\tau$  values (the inertial or mesoscale range), we expect  $SF_\nu(\tau) \propto \tau^{H\nu}$ .<sup>26,27</sup> See Fig. 15.

The best fit is obtained focusing on the intermediate range and discarding the initial (low  $\tau$ ) and final ranges (high  $\tau$ ).  $H \sim 1$  is expected for times smaller than the decorrelation time of the turbulence, while  $H \sim 0$  for times of the order of the confinement time. Again, the intermediate value of  $H$  is the interesting one.

However, the SFs of some specific tracers have a peak around  $\tau = 10 \mu s$  (Fig. 16), corresponding to approximately one period of the fast oscillations observed in the region  $r/a < 0.35$  (see above). Therefore, we can distinguish two classes of tracers and their corresponding SFs. Type I corresponds to tracers that do not enter the core region

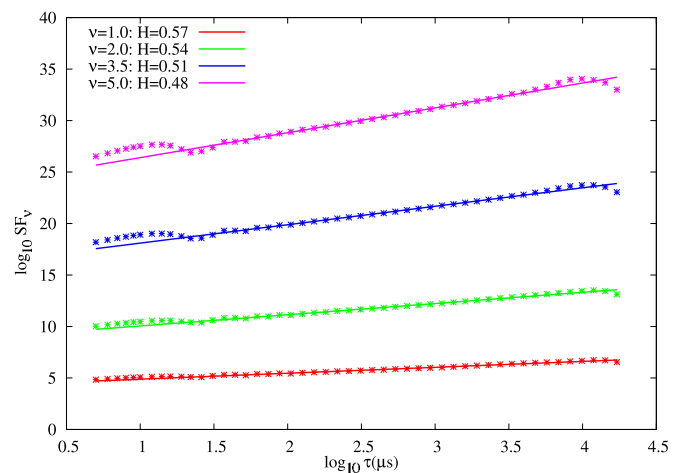


FIG. 16. (Color online) Type II SFs for a single tracer, with different  $\nu$ 's and fits.

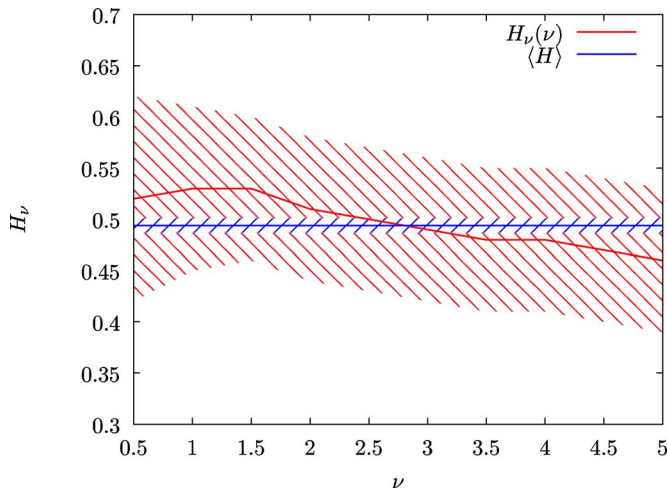


FIG. 17. (Color online)  $H_\nu$  as a function of  $\nu$ . Type I and II SFs are considered.

$r/a < 0.35$ , and in this case the SF has the expected three well separated and differentiated intervals, while the intermediate region has  $H \sim 0.5$ . Type II corresponds to tracers that enter the core region, if only for a small part of their trajectory. There, they experience large amplitude and strongly oscillating radial velocities. This fact is reflected in the SF that shows the mentioned peak at small  $\tau$ , and does not possess the initial  $\tau$  range with  $H_0 \sim 1$ .

The measured Hurst exponent of the intermediate range of type I and II SFs is approximately the same. The average  $H_\nu$  value decays slightly with  $\nu$  (Fig. 17). If significant, this might indicate some degree of multifractality. However, we consider that  $H_\nu$  is constant within the error. In the H-mode, we obtain  $\langle H \rangle = 0.494 \pm 0.007$ , very similar to the L-mode result,  $\langle H \rangle = 0.452 \pm 0.019$ .

For type I SFs (for which the slope change can be more clearly appreciated), the transition from the initial ballistic time range to the intermediate mesoscale range occurs for  $\tau > \tau_H = 30 \mu\text{s}$ , the same value as found using the RS analysis (see above). Again, this value is smaller than the L-mode result by a factor of 3.

### 3. Cumulative velocity

Finally, we test the presence of long range correlations by studying the distribution  $p(d)$  of the total displacement  $d$  in a given time  $\tau_0$ . For long enough time intervals  $\tau_0$ ,  $p(d)$  is expected to decay in a similar fashion as the step size pdf. If the latter is non-Gaussian Lévy with decay index  $\alpha$ , then  $p(d) \propto d^{-1-\alpha}$ .<sup>28</sup>

We have computed this pdf for different values of  $\tau_0$ . Figure 18 shows how the tail of the distribution becomes heavier as  $\tau_0$  increases. The tail of the distribution is only observed toward the outside because of the transport barrier at  $r/a \approx 0.3$  and the inward drift. By comparison, note that the L-mode curve peaks toward positive values of  $\Delta(r/a)$ , while the tail is observed inwards<sup>18</sup> due to the opposite drift. The shape of the propagator (Fig. 6) in L- and H-mode corresponds closely to the pdf of the displacements.

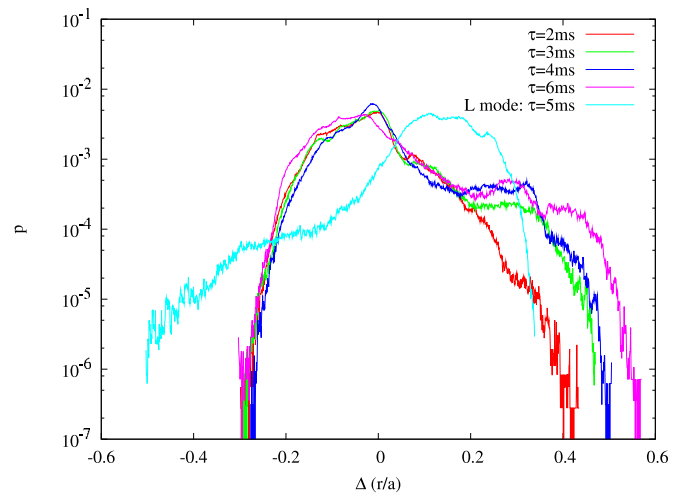


FIG. 18. (Color online) L- and H-mode cumulative velocities pdf.

The best fits of a power law in both L- and H-modes are shown in Fig. 19. The curves are displaced so that they peak at  $\Delta(r/a) = 0.0$ , and a power law appears as a straight line.

In this case, the fit length [cf. Eq. (1)] for the L-mode is almost a decade  $L_{\text{fit,L}} = 0.75$ . In the H-mode, depending on  $\tau_0$ ,  $L_{\text{fit,H}}$  varies from 0.39 to 0.47, which we consider insufficient for drawing a conclusion.

### D. Tracer motion

It is immediately clear that the transport of tracers in the L- and H-modes is qualitatively different.

#### 1. Step asymmetry

The first evidence for this is obtained when quantifying the mean step size of positive and negative steps according to radius (Fig. 20). For the calculation method, refer to Ref. 1.

In the L-mode case, a strong asymmetry is observed, which can be understood if transport is strongly nonlocal in the sense that the local asymmetry of the step distribution

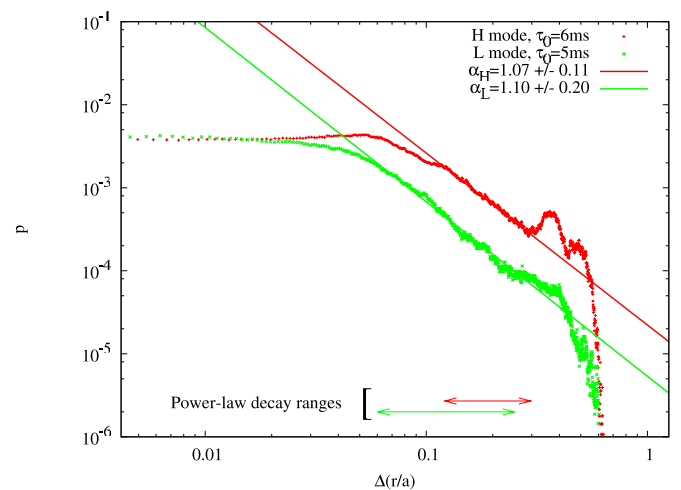


FIG. 19. (Color online) L- and H-mode cumulative velocities and fits (log-log).

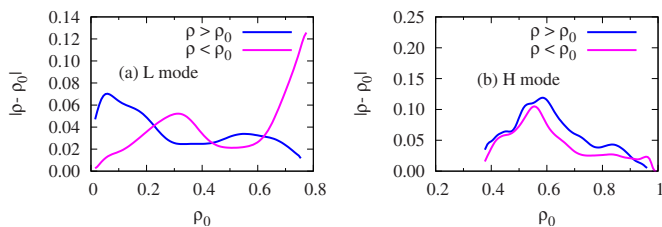


FIG. 20. (Color online) Positive and negative mean step size profiles.

depends on conditions (such as boundary conditions) that are not strictly local. This asymmetry almost completely disappears in the H-mode, where the mean positive and negative steps have practically the same value. We interpret this in the sense that transport in the H-mode is much more local in nature, and randomization is more pronounced (i.e., turbulent eddies, if present, have a reduced size, and streamers, if present, are less important in the H-mode).

### 2. Step size profiles

Here we show (Fig. 21) the mean square displacement profiles in the L- and H-mode runs. Note how, in both plots, the increase in  $\langle \Delta \rho^2 \rangle$  is accompanied by a decrease in the number of steps. As expected, in the plasma regions where steps are small, the number of tracer steps is higher. L- and H-mode  $\langle \Delta \rho^2 \rangle(r/a)$  profiles have several differences. The mean square displacement is longer in H-mode, by a factor of around 10. However the number of steps is reduced by the same factor of 10, being the H-mode curve much more scattered than the L-mode curve. In H-mode,  $\langle \Delta \rho^2 \rangle$  peaks at  $r/a \sim 0.6$ . In L-mode it keeps constant while it is far enough from the transport barrier in  $r/a = 0.8$ .

### 3. Trapping time profiles

We have also computed the mean trapping time as a function of the radial position in L- and H-modes (Fig. 22). This quantity and  $\langle \Delta \rho^2 \rangle(r/a)$  behave similarly: The maximum peaks at  $r/a \sim 0.6$  in H-mode, while it increases dramatically at  $r/a \sim 0.7$  in the L-mode run, with very few events. The waiting times are longer in H-mode, excepting the outer region.

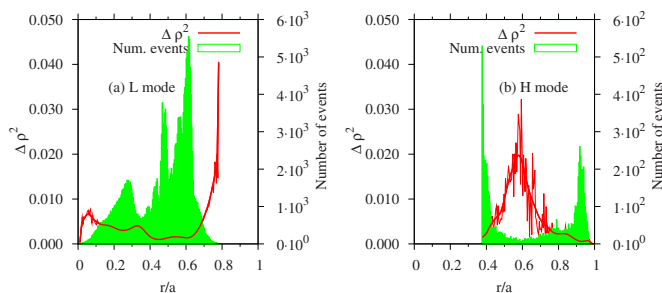


FIG. 21. (Color online) Profiles of the L- and H-mode mean square displacements, and number of displacements.

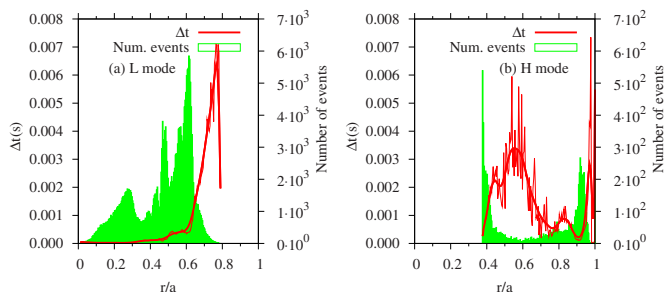


FIG. 22. (Color online) Profiles of the L- and H-mode mean trapping times, and number of displacements.

### 4. Fractional diffusion coefficient

In the fractional diffusion scenario, with nonstandard  $\alpha$  and  $\beta$  values, the role of the diffusion coefficient is played by  $D_{\alpha,\beta} = \Delta x^\alpha / \Delta t^\beta$ .<sup>17</sup> In L-mode the tracer diagnostics worked rather well, being the fractional parameters  $\alpha_L \approx 1$ ,  $\beta_L \approx 1/2$ , and  $H_L \approx 1/2$ . In H-mode, only  $H_H \approx 1/2$  can be considered to be robust. Assuming  $\beta_H \approx 1/2$  (see below), we conclude that the fractional parameters do not change significantly across the L-H transition. Using these values, we have computed the corresponding effective diffusion coefficient in the L- and H-modes (Fig. 23).

In the region of interest (remember that the L-mode analysis is valid mainly in  $0.35 \leq r/a \leq 0.8$ , while in H-mode it is restricted to the range  $0.35 \leq r/a < 1$ )  $D_{\alpha,\beta}$  decreases monotonically with  $r/a$  in L-mode, while it shows a non-trivial structure in H-mode, peaking at  $r/a \sim 0.6$ , where the number of events is low. Apparently, in H-mode, there are two “privileged” radial positions where tracers tend to linger, corresponding to the  $D_{\alpha,\beta}$  minima at  $r/a \sim 0.4$  and  $r/a \sim 0.8$ .

### 5. Impact of ELMs

Another interesting feature of the tracer motion in the H-mode is their behavior in the pedestal zone, where ELMs dominate (Fig. 24). Inside the pedestal zone ( $r/a < 0.85$ , indicated by the blue zone), the tracer motion can be recognized as a random walk (see below). However, in the pedestal zone, motion is dominated by the quasiperiodic ELM relaxation phenomena (with approximate period  $\tau_{ELM}$ ), between which the particles are virtually motionless (radially).

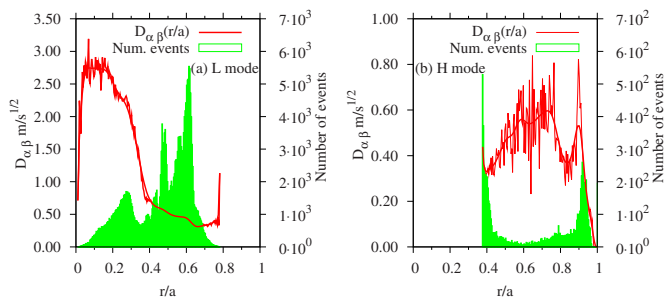


FIG. 23. (Color online) Profiles of the L- and H-mode fractional diffusion coefficients, and number of events.

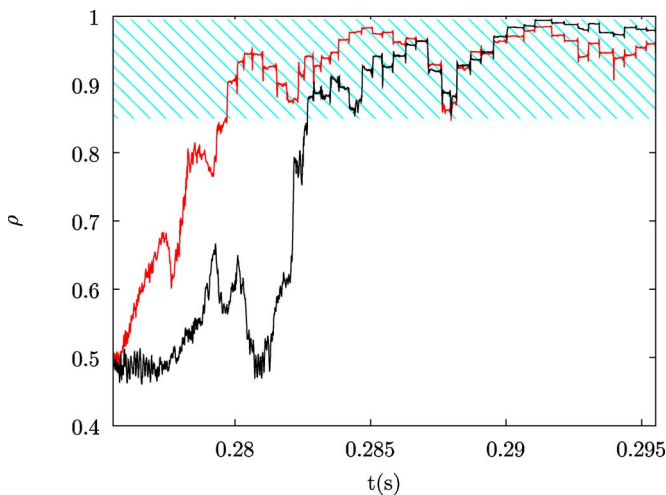


FIG. 24. (Color online) Radial trajectories of two tracers in the ELMs region.

#### IV. DISCUSSION

Several analysis techniques for the detection of long range/long time correlations and Lévy distribution parameters have been applied to the study of L- and H-mode simulations in CUTIE. It is the first time such a comparison is attempted using these techniques.

Transport in the L- and the H-modes is known to be significantly different; in particular, anomalous transport is known to be less dominant in H-mode. However, not much is known about the behavior of the anomalous transport parameters ( $\alpha$ ,  $\beta$ , and  $H$ ) across the confinement transition, and this is the subject of study of this paper.

One problem we have encountered is the distortion of the distributions due to finite-size effects, complicating the analysis. The propagator is distorted by particle drift and transport barriers in both the L- and H-modes, but in the latter case the distortion is such that it becomes impossible to determine a precise value of  $\alpha$ , in spite of the fact that we have attempted to use a variety of techniques to extract this number. However, results for  $\beta$  and  $H$ , together with the relationship  $\alpha = \beta/H$ , indicate that the transport parameters are quite similar in L- and H-modes as Table I shows. Note that the L-mode parameters in the table have been derived from different independent techniques, while the H-mode  $\alpha$  value is inferred from its relationship with the other outputs:  $\beta \approx \frac{1}{2}$  and  $H \approx \frac{1}{2}$ ; thus  $\alpha \approx 1$ . Note, however, that the quality of the fits is better in the L-mode than in the H-mode for all diagnostics used. Furthermore, the value  $\beta_H \approx \frac{1}{2}$  rests on the application of a single diagnostic (the waiting time pdf), unlike the L-mode results<sup>1</sup> that benefit from the mutual

TABLE I. Compilation of results.

	L-mode	H-mode
$\alpha$	1.3	1
$\beta$	1/2	1/2
$H$	1/2	1/2

confirmation among a number of diagnostics. The H-mode result for  $H$  is more robust, as it is confirmed by two different diagnostics.

Apart from the measurement of  $\alpha$ ,  $\beta$ , and  $H$ , we have observed some significant differences between the two cases.

- (1) The mean step size is larger in the H-mode. This explains the problems associated with the finite size of the system and the distortion of the pdfs. However, this does not mean that the diffusion is larger in the H-mode. Rather, it was found that the rate of increase in the square width of the tracer pdf (the effective diffusion coefficient) is smaller in the H-mode by a factor of 2. This is interpreted as being due to the increased importance of particle trapping, thus impeding spreading, while allowing large excursions between the successive trappings.
- (2) The mean step size, strongly asymmetric for positive/negative steps in L-mode, is rather symmetric in the H-mode. We interpret this to mean that transport is more local in the H-mode. This would be consistent with the idea of radially localized trapping regions that serve to disconnect remote regions, and thus make transport less subject to influences across long distances. The same is suggested by the presence of two separate plasma regions where the effective diffusion coefficient is small. Further work would be needed to confirm this hypothesis.
- (3) The inward propagation of the quasiperiodic events, with a higher velocity in the L-mode than the H-mode, suggests that the L-mode profile is stiffer—although the reduced depth of the propagation indicates that the stiff region is wider in the H-mode. This seems to be in accord with the fact that nonlocality is more important in L-mode than in H-mode (at least, in the stiff zone) and with the existence of (minor) transport barriers or trapping regions in the H-mode. In any case, the transport is influenced but not dominated by the quasiperiodic events since transport is not ballistic (which would yield  $H \approx 1$ ).
- (4) The RS analysis shows that the separation point between the first and second logarithmic slopes for the H-mode,  $\tau_H$ , is three times smaller than the same quantity in L-mode,  $\tau_L$ . The same conclusion is obtained studying the SFs, although only type I SFs allow obtaining the  $\tau_H$  time. This was interpreted as a reduction in the turbulence decorrelation time in H-mode, in accord with many experimental and theoretical results obtained previously.

Finally, we have also shown what the effect of the ELMs on the tracer trajectories is (cf. the peak at  $\Delta t \approx 0.4$  ms  $\approx \tau_{ELM}$  in Figs. 12 and 13).

#### V. CONCLUSIONS

The radial transport of tracer particles in our H-mode simulation with CUTIE has been studied with different analysis techniques. Finite-size effects imposed restrictions on the precision of the determination of the self-similar scaling

parameters. However, within the error bars, no significant differences were found between the scaling parameters of the H-mode and those of the L-mode studied previously. This is the first time such a comparison is made based on these techniques.

In spite of the above, the L- and H-mode simulations do show important differences in other respects. In the H-mode, the mean step is larger, and yet the effective diffusion coefficient is smaller. This apparent contradiction is resolved by the observation that the turbulence decorrelation time is reduced in the H-mode, and that the H-mode step distributions are much more symmetric (with regard to positive/negative steps). These observations are consistent with the hypothesis that the L-mode profile is stiffer, as suggested by the increased propagation velocity of perturbations, and therefore more nonlocal.

We note that these observations are consistent with the observation made in another plasma simulation that the transport gradually becomes local as the plasma beta increases.<sup>29</sup> In the latter reference, the increase in beta is not accompanied by an L-H transition.

In CUTIE, the plasma beta also is slightly increased after the transition: The density increases while the decrease in electron temperature is partially compensated by the increase in ion temperature (while  $n_e = n_i$ ); the net effect is that the plasma beta rises from  $\beta_{\text{plasma,L}} \approx 0.55$  in L-mode to  $\beta_{\text{plasma,H}} \approx 0.75$  in H-mode.

In all, interesting insight into the complexity of transport is gained using these techniques. We believe that it would be very useful to extend these analyses to other types of transport codes (e.g., gyrokinetic codes) in order to improve the understanding of anomalous transport. Also, more realistic particles could be used (with mass and charge) in order to compare simulation results with actual measurements of, e.g., impurity transport.

## ACKNOWLEDGMENTS

The authors would like to thank the TJ-II Team for their support, and R. Sánchez and B. Carreras for stimulating discussions. This research was sponsored in part by the Dirección General de Investigaciones Científicas y Tecnológicas (DGICYT) of Spain under Project Nos. ENE2006-15244 and ENE2009-07247. A. Thyagaraja's research was funded jointly by United Kingdom Engineering and Physical Sciences Research Council under Grant No. EP/G003955 and the European Communities under the contract of Association between EURATOM and CCFE. The views and opinions

expressed herein do not necessarily reflect those of the European Commission.

- <sup>1</sup>G. Sánchez Burillo, B. Ph. van Milligen, and A. Thyagaraja, *Phys. Plasmas* **16**, 042319 (2009).
- <sup>2</sup>A. Thyagaraja, P. Knight, M. de Baar, G. Hogewij, and E. Min, *Phys. Plasmas* **12**, 090907 (2005).
- <sup>3</sup>B. A. Carreras, V. Lynch, and G. Zaslavsky, *Phys. Plasmas* **8**, 5096 (2001).
- <sup>4</sup>L. García and B. A. Carreras, *Phys. Plasmas* **13**, 022310 (2006).
- <sup>5</sup>D. del-Castillo-Negrete, B. A. Carreras, and V. Lynch, *Phys. Plasmas* **11**, 3854 (2004).
- <sup>6</sup>J. Mier, R. Sánchez, L. García, D. Newman, and B. A. Carreras, *Phys. Plasmas* **15**, 112301 (2008).
- <sup>7</sup>D. del-Castillo-Negrete, B. A. Carreras, and V. Lynch, *Phys. Rev. Lett.* **94**, 065003 (2005).
- <sup>8</sup>R. Sánchez, D. E. Newman, J. N. Leboeuf, V. K. Decyk, and B. A. Carreras, *Phys. Rev. Lett.* **101**, 205002 (2008).
- <sup>9</sup>G. Spizzo, R. B. White, S. Cappello, and L. Marrenelli, *Plasma Phys. Controlled Fusion* **51**, 124026 (2009).
- <sup>10</sup>E. Montroll and G. Weiss, *J. Math. Phys.* **6**, 167 (1965).
- <sup>11</sup>W. Shugard and H. Reiss, *J. Chem. Phys.* **65**, 2827 (1976).
- <sup>12</sup>B. Ph. van Milligen, R. Sánchez, and B. A. Carreras, *Phys. Plasmas* **11**, 2272 (2004).
- <sup>13</sup>V. Kenkre, E. Montroll, and M. Shlesinger, *J. Stat. Phys.* **9**, 45 (1973).
- <sup>14</sup>J. Klafter and R. Silbey, *Phys. Rev. Lett.* **44**, 55 (1980).
- <sup>15</sup>B. Gnedenko and A. Kolmogorov, *Limit Distributions for Sums of Independent Random Variables* (Addison-Wesley, Reading, MA, 1954), p. 162.
- <sup>16</sup>R. Metzler and J. Klafter, *Phys. Rep.* **339**, 1 (2000).
- <sup>17</sup>R. Sánchez, B. A. Carreras, and B. Ph. van Milligen, *Phys. Rev. E* **71**, 011111 (2005).
- <sup>18</sup>P. Mantica, A. Thyagaraja, J. Weiland, G. Hogewij, and P. Knight, *Phys. Rev. Lett.* **95**, 185002 (2005).
- <sup>19</sup>L. Garzotti, X. Garbet, A. Thyagaraja, M. de Baar, D. Frigione, P. Mantica, V. Parail, B. Pégourié, L. Zabeo, and JET EFDA contributors, *Nucl. Fusion* **45**, 73 (2005).
- <sup>20</sup>R. Pánek, O. Bilyková, V. Fuchs, M. Hron, P. Chráska, P. Pavlo, J. Stöckel, J. Urban, V. Weinzettl, J. Zajac and F. Žáček, *Czech. J. Phys.* **56**, B125 (2006).
- <sup>21</sup>A. Thyagaraja, P. Knight, and N. Loureiro, *Eur. J. Mech. B/Fluids* **23**, 475 (2004).
- <sup>22</sup>G. Hogewij, A. Oomens, C. Barth, M. Beurskens, C. Chu, J. van Gelder, J. Lok, N. Lopes Cardozo, F. Pijper, R. Polman, and J. Rommers, *Phys. Rev. Lett.* **76**, 632 (1996).
- <sup>23</sup>M. de Baar, A. Thyagaraja, G. Hogewij, P. Knight, and E. Min, *Phys. Rev. Lett.* **94**, 035002 (2005).
- <sup>24</sup>A. Thyagaraja, M. Valovic, and P. Knight, "Global two-fluid turbulence simulations of L-H transitions and ELM dynamics in the COMPASS-D tokamak," *Phys. Plasmas* (to be published).
- <sup>25</sup>B. A. Carreras, B. Ph. van Milligen, M. Pedrosa, R. Balbín, C. Hidalgo, D. Newman, E. Sánchez, M. Frances, I. García-Cortés, J. Bleuel, M. Endler, S. Davies, and G. Matthews, *Phys. Rev. Lett.* **80**, 4438 (1998).
- <sup>26</sup>M. Gilmore, C. Yu, T. Rhodes, and W. Peebles, *Phys. Plasmas* **9**, 1312 (2002).
- <sup>27</sup>C. Yu, M. Gilmore, W. Peebles, and T. Rhodes, *Phys. Plasmas* **10**, 2772 (2003).
- <sup>28</sup>R. Sánchez, B. A. Carreras, D. Newman, V. Lynch, and B. Ph. van Milligen, *Phys. Rev. E* **74**, 016305 (2006).
- <sup>29</sup>L. García, B. A. Carreras, I. Llerena, and I. Calvo, *Phys. Rev. E* **80**, 046410 (2009).